Electronic Supplementary Material (ESI) for Energy & Environmental Science.

Supporting Information

Transient, *in situ* Synthesis of Ultrafine Ruthenium Nanoparticles for a High-rate Li-CO_2 Battery

Yun Qiao,[1‡] Shaomao Xu,[1‡] Yang Liu,[1] Jiaqi Dai,[1] Hua Xie,[1] Yonggang Yao,[1] Xiaowei Mu,[2] Chaoji Chen,[1] Dylan Jacob Kline,[3] Emily M. Hitz,[1] Boyang Liu,[1] Jianwei Song,[1] Ping He,[2] Michael R. Zachariah,[3] Liangbing Hu*[1]

[1] Department of Materials Science and Engineering, University of Maryland, College Park, Maryland, 20742, USA.

[2] College of Engineering and Applied Sciences, Nanjing University, Nanjing, 210093, China.

[3] Department of Chemistry and Biochemistry, University of Maryland, College Park, Maryland, 20742, USA.

[*] Email: binghu@umd.edu

[‡] These authors contributed equally to this work.

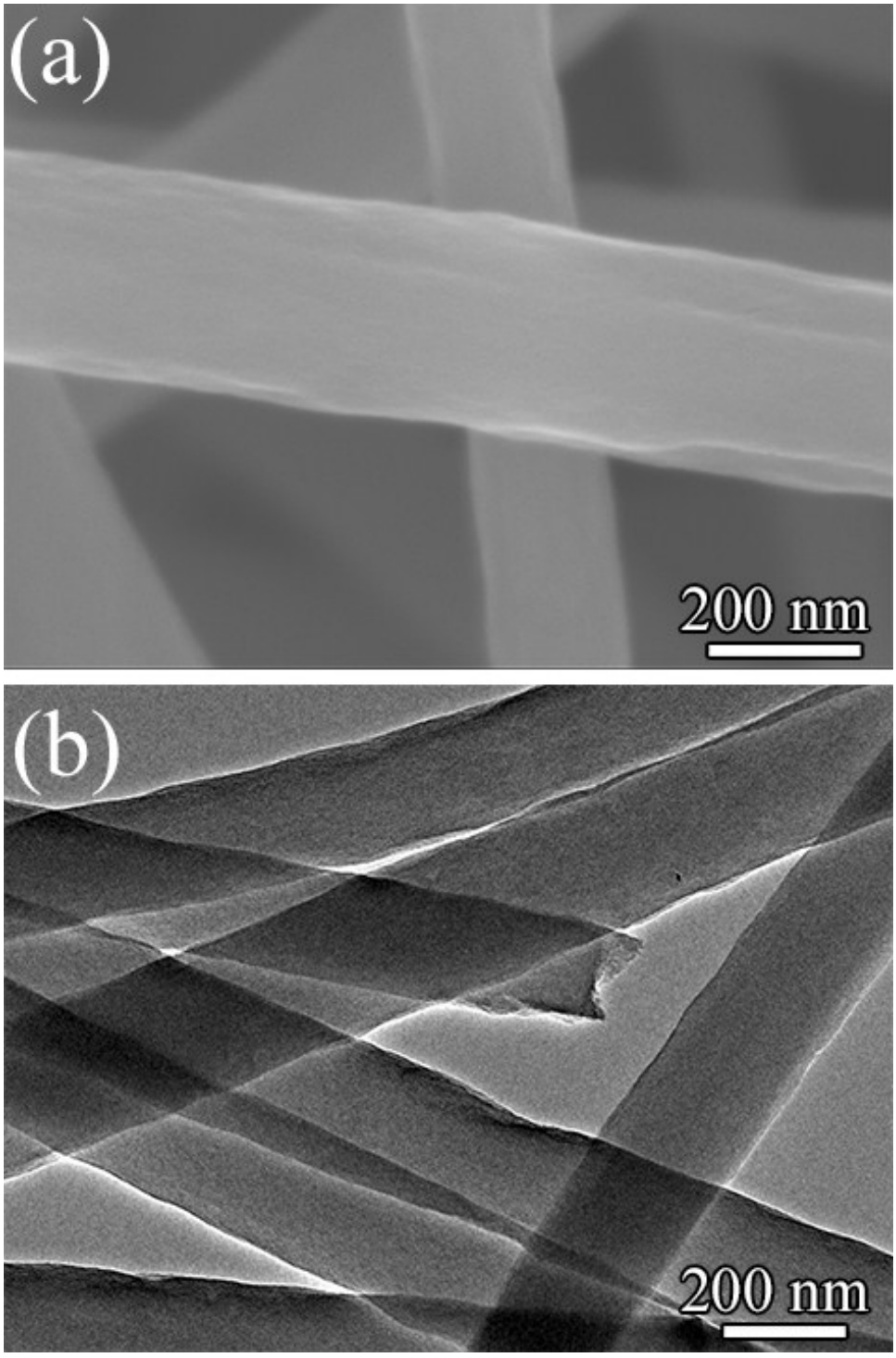

Figure S1. (a) SEM and (b) TEM images of pristine carbon nanofibers, showing the smooth surface without any pores or holes.

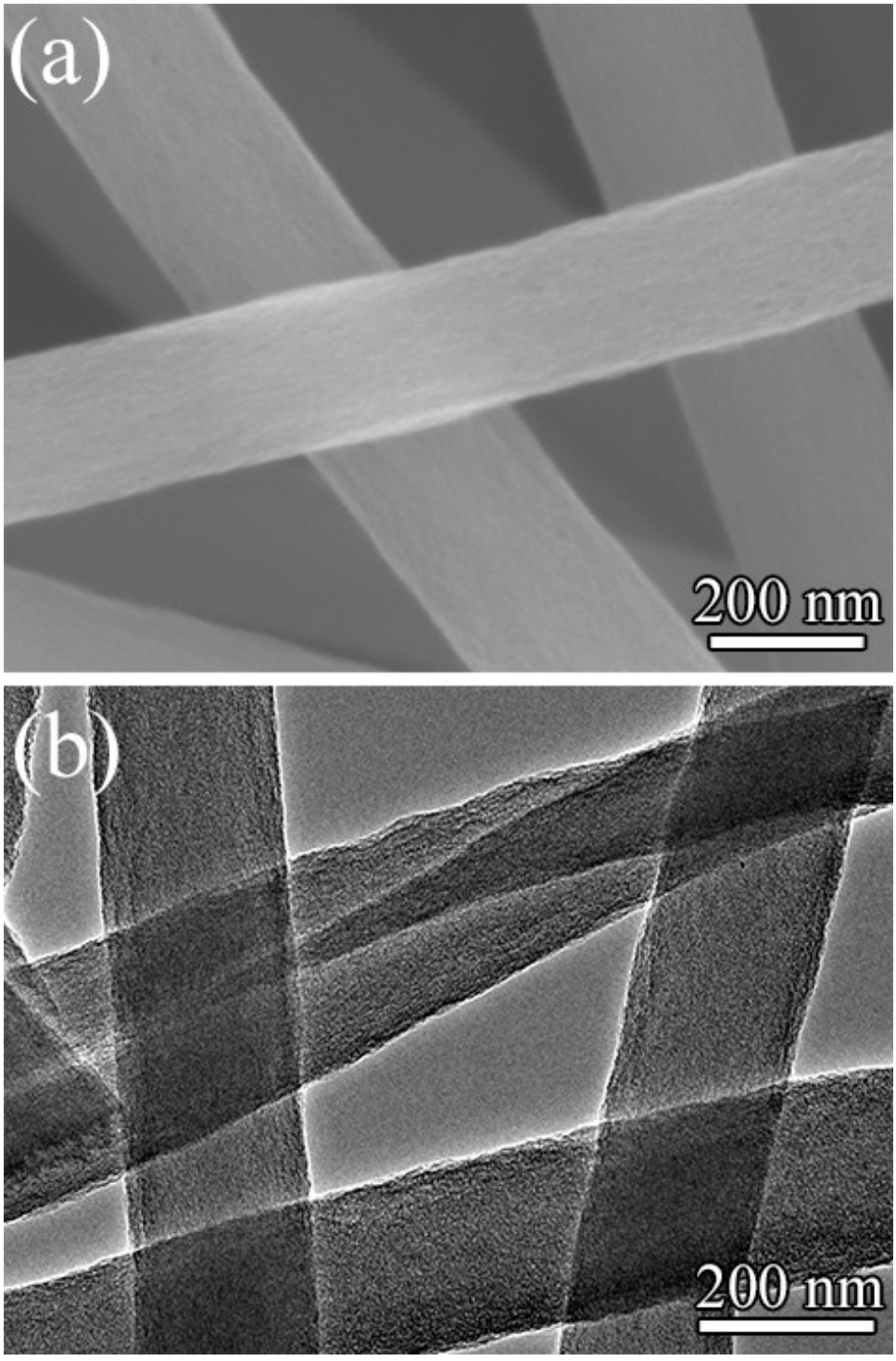

Figure S2. (a) SEM and (b) TEM images of the ACNFs, showing how the surface of the CNFs become rough and porous after CO_2 gasification.

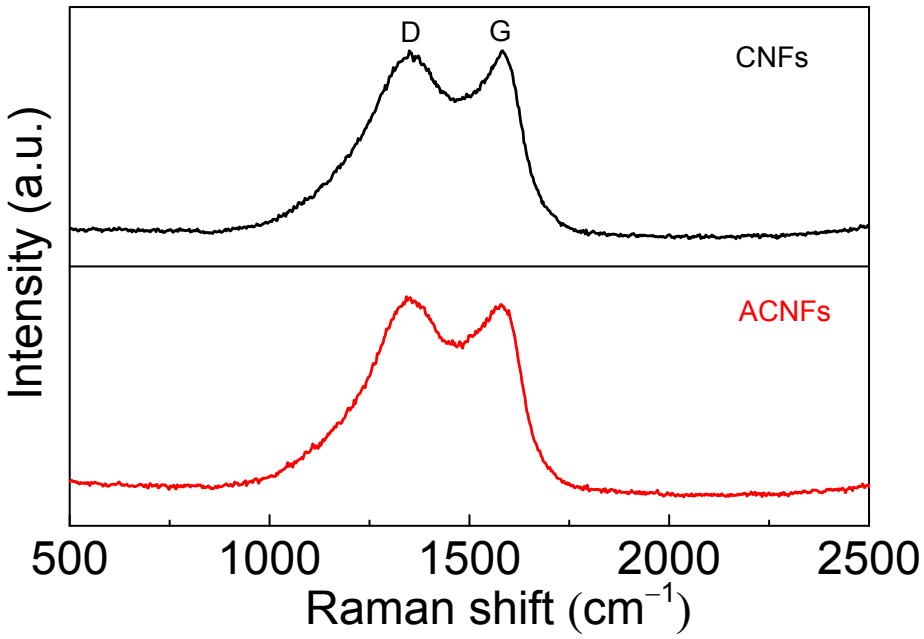

Figure S3. Raman spectra of CNFs and ACNFs, featuring peaks at 1353 and 1580 cm^{-1} that correspond to the D band (disordered or defective carbon structure) and G band (graphitic sp^2 carbon structures), respectively. The I_D/I_G ratio increases from 0.97 (CNFs) to 1.03 (ACNFs), indicating more defective sites in ACNFs after CO_2 gasification compared to CNFs.

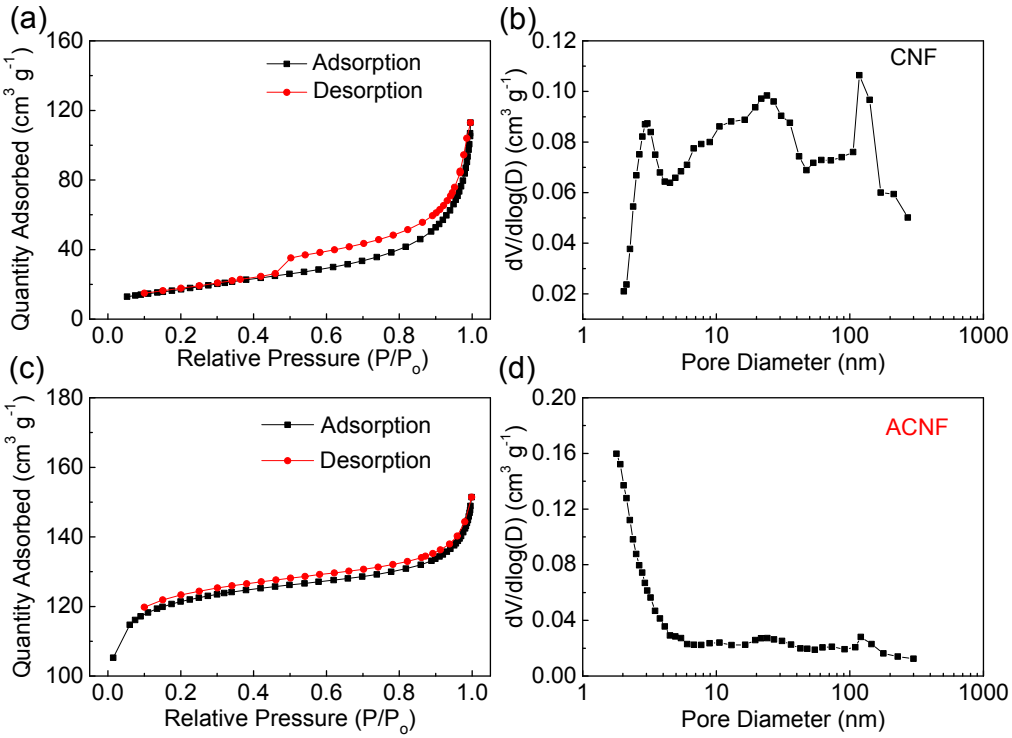

Figure S4. Nitrogen adsorption-desorption isotherms and pore size distribution of (a, b) CNFs and (c, d) ACNFs. The BET surface areas for the CNFs and ACNFs are 63.18 and 379.91 $m^2\ g^{-1}$, while the t-Plot micropore volumes are 3.85×10^{-3} and 136.74×10^{-3} $cm^3\ g^{-1}$, respectively. These results demonstrate that the surface area and pore volume for the ACNFs are enhanced after CO_2 activation, which could provide more adsorption sites for the ruthenium salt and deposition sites for ultrafine Ru nanoparticles, not only on the surface but also inside the ACNFs.

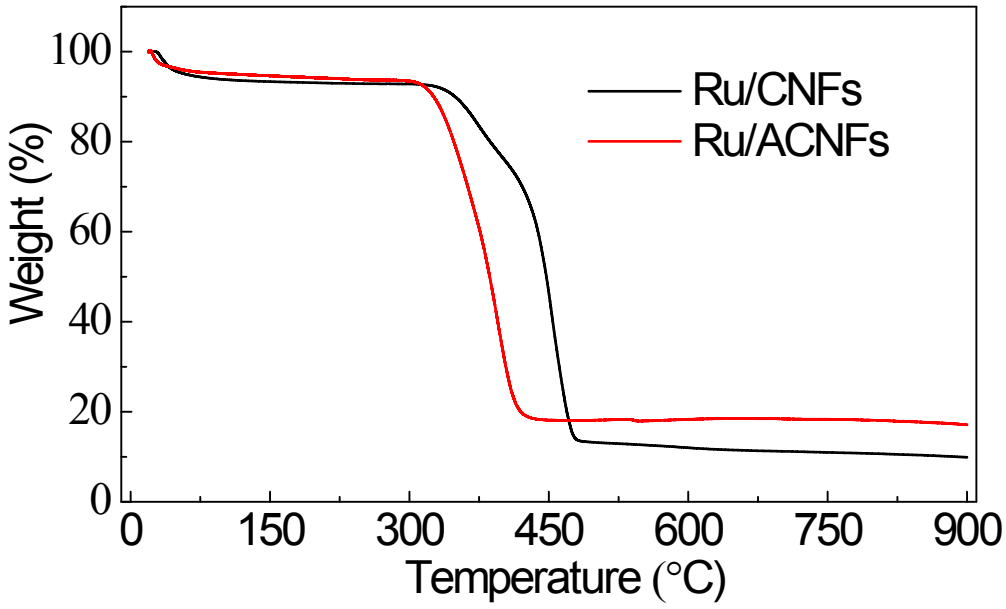

Figure S5. TGA curves of the Ru/CNFs and Ru/ACNFs from room temperature to 900 °C at a heating rate of 10 °C min^{-1} in air atmosphere.

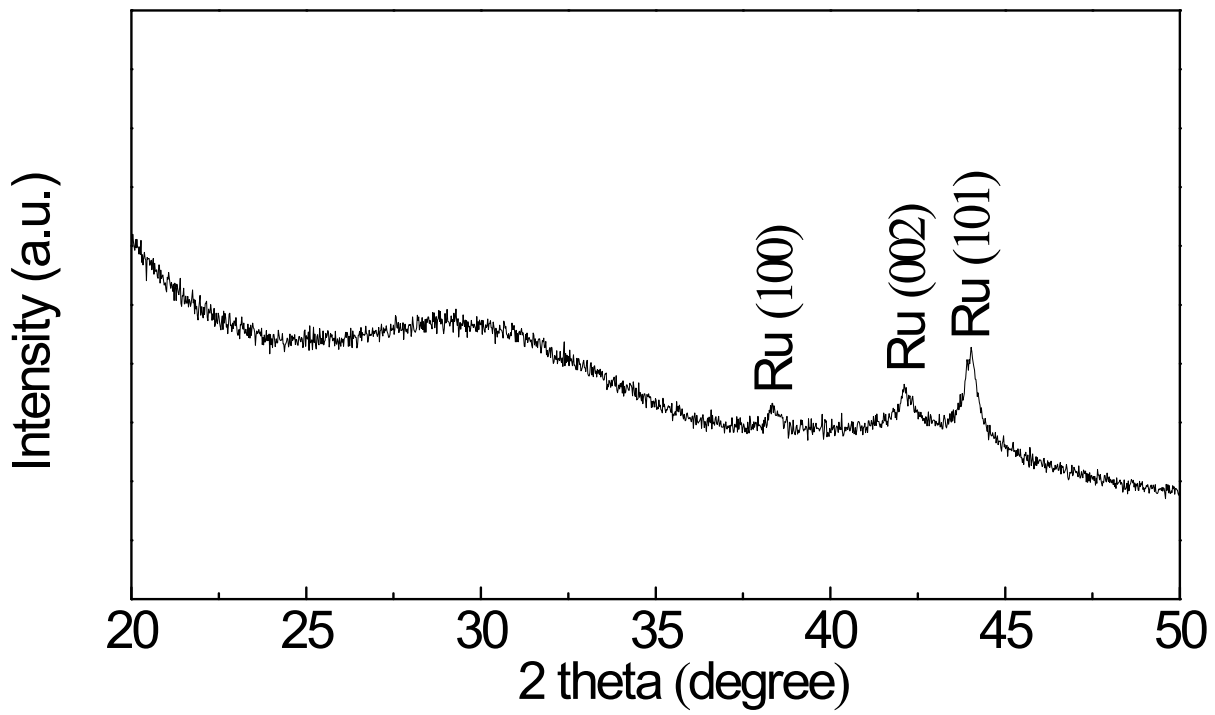

Figure S6. XRD pattern of the Ru/ACNFs electrode, which demonstrates the Ru nanoparticles are successfully anchored on the activated CNFs.

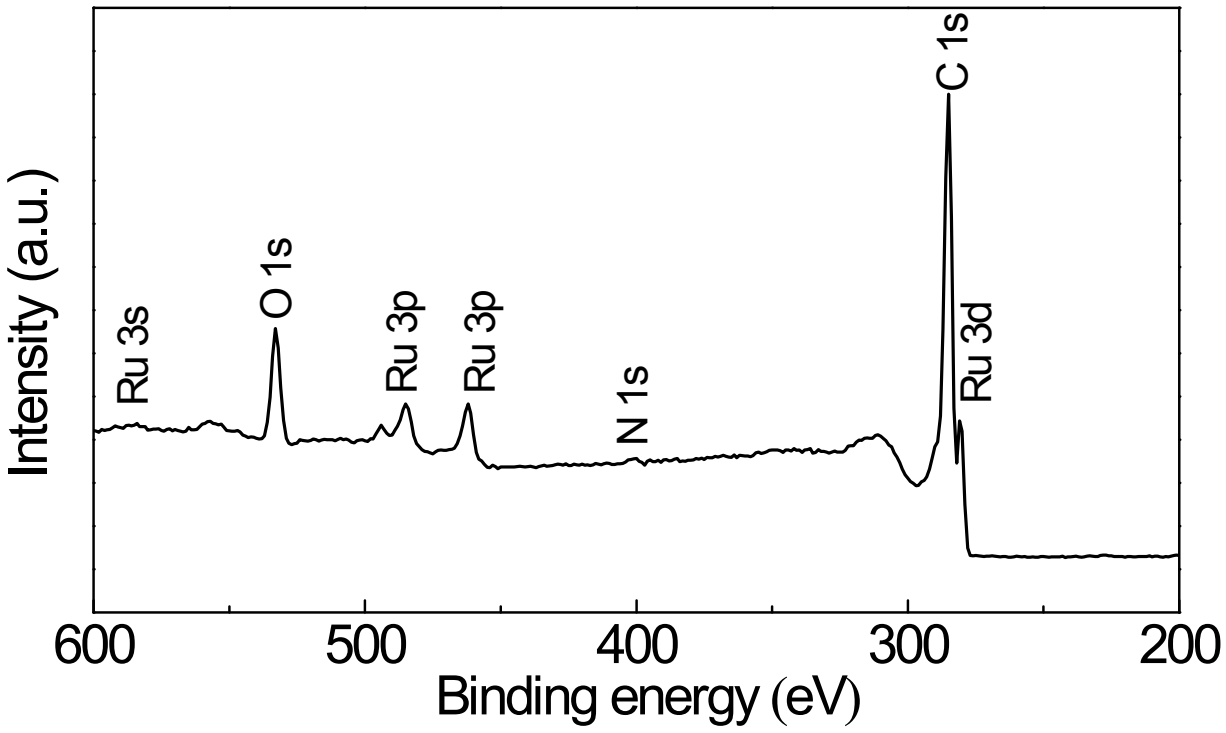

Figure S7. XPS spectrum of the Ru/ACNF cathode, further certifying it is composed of C, Ru, N, and O.

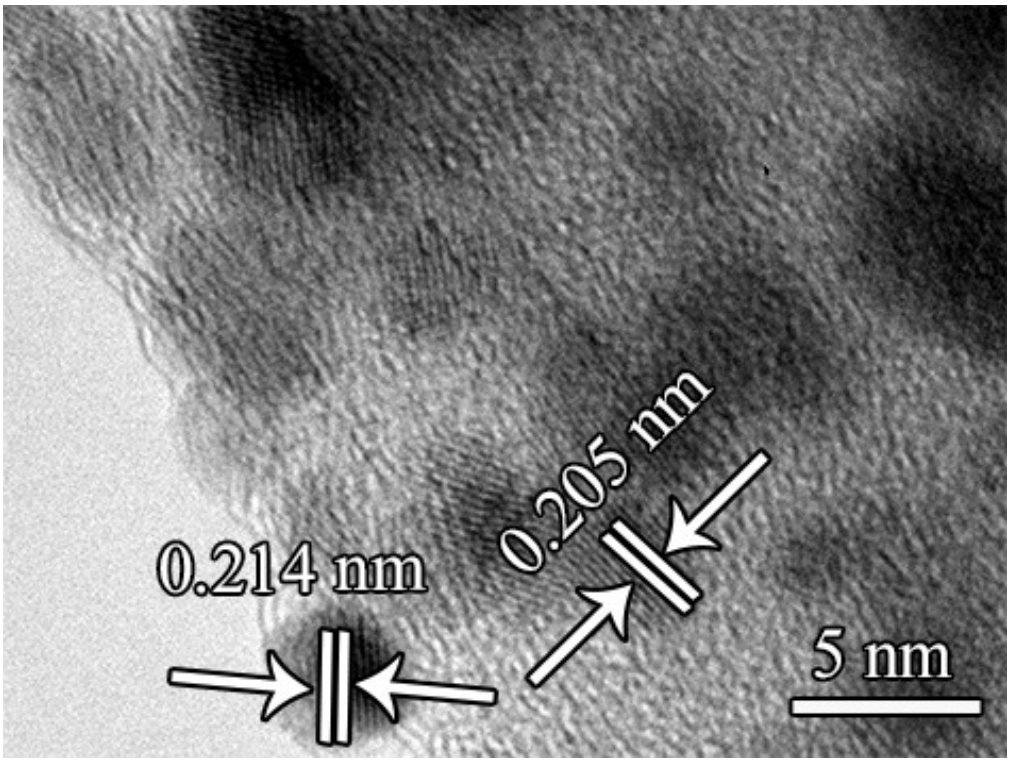

Figure S8. High resolution TEM image of the Ru/ACNF electrode.

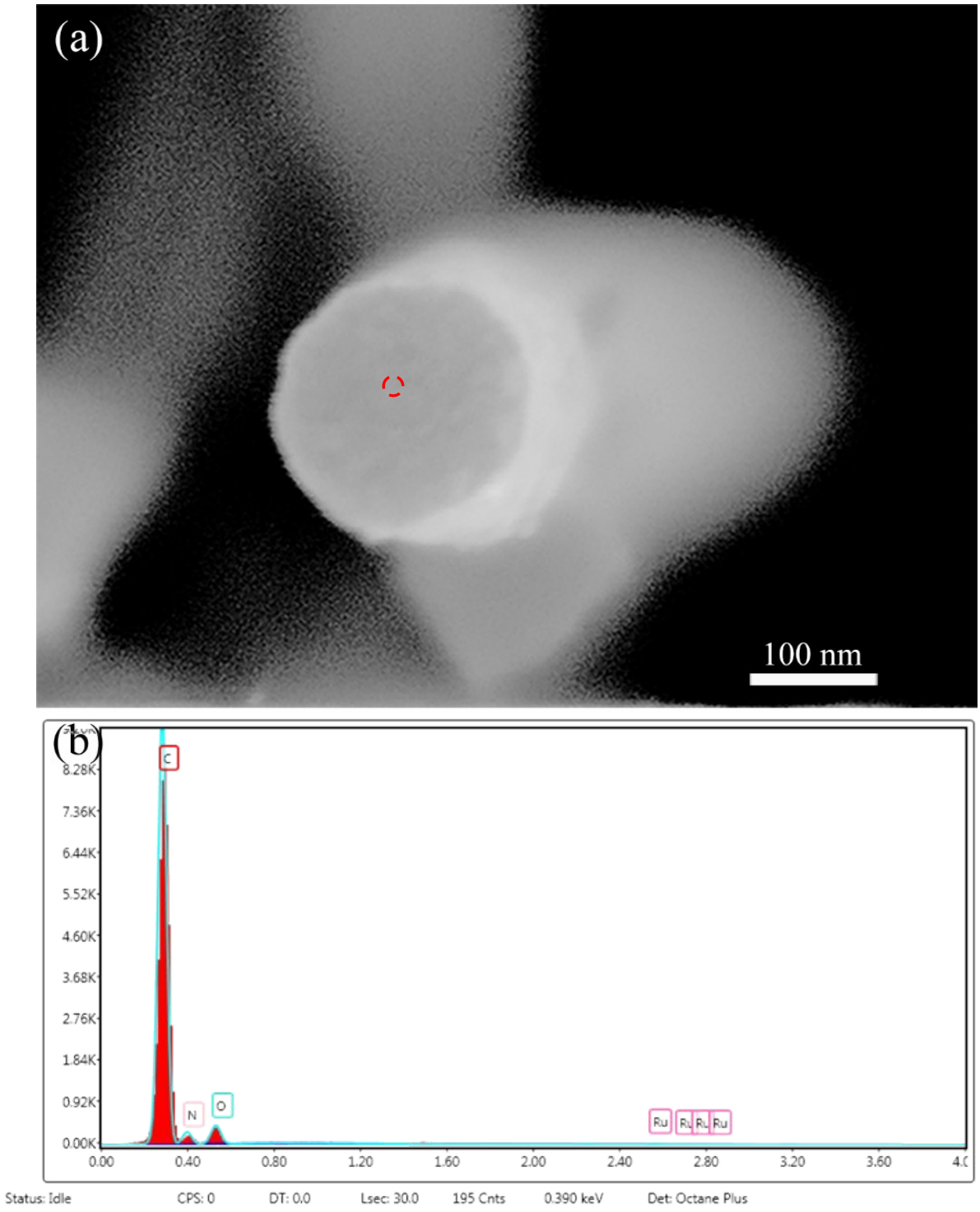

Figure S9. (a) Cross-sectional SEM image and (b) the corresponding EDX spectrum of the Ru/CNF electrode, indicating that the Ru nanoparticles are not deposited on the interior of the fibers.

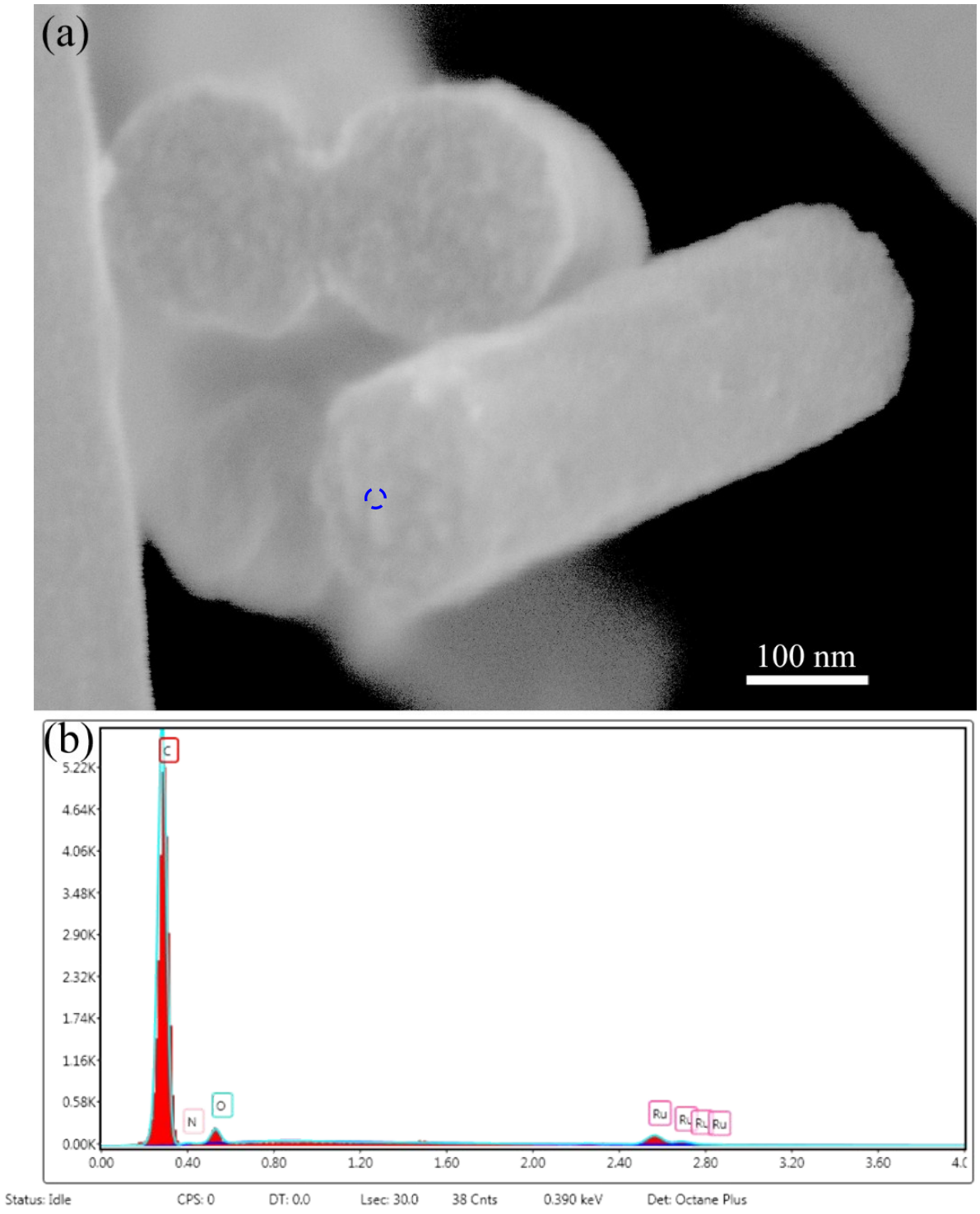

Figure S10. (a) Cross-sectional SEM image and (b) the corresponding EDX spectrum of the Ru/ACNF electrode, confirming that Ru nanoparticles can be successfully deposited not only on the surface of the fibers but also within their interior.

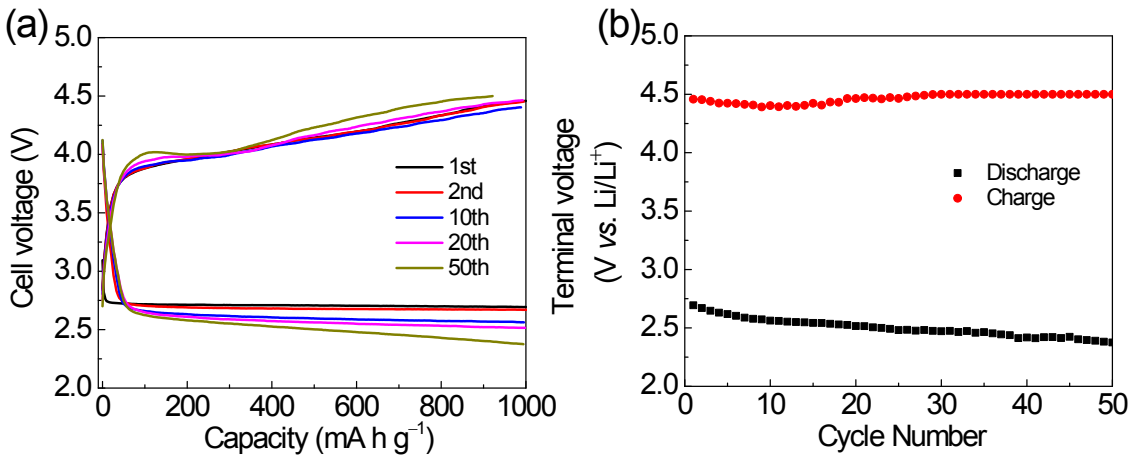

Figure S11. The electrochemical performance of the ACNF cathode at a current density of 0.1 A g^{-1} in a Li-CO_2 battery. (a) Charge/discharge curves of the ACNF cathode at the 1st, 2nd, 10th, 20th, and 50th cycles with a limiting capacity of 1000 mA h g^{-1}. (b) The corresponding discharge and charge terminal voltages upon cycling.

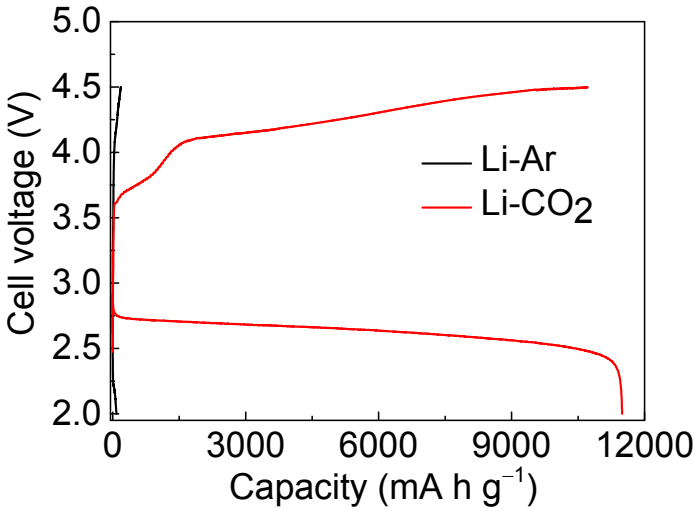

Figure S12. Full charge and discharge profiles of the Ru/ACNF cathode at a current density of 200 mA g^{-1} in Li-Ar and Li-CO_2 batteries.

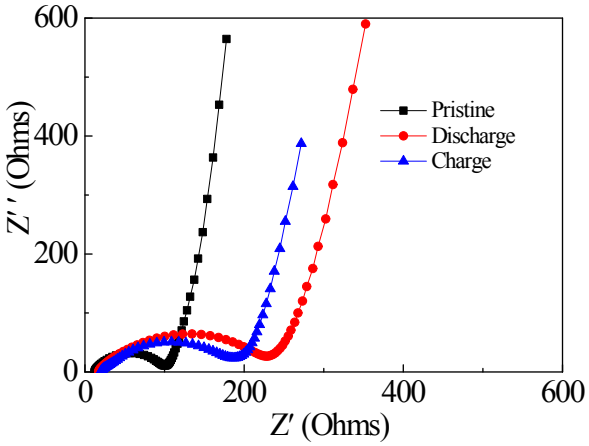

Figure S13. The electrochemical impedance spectra for the initial and cycled Ru/ACNF cathode.

The Nyquist plots at different states are almost the same, demonstrating a depressed semicircle in the high-middle frequency region and an oblique straight line in the low frequency range. These plots with small semicircles suggest a low resistance of ~100 Ω, which can be attributed to the fact that the Ru/ACNF electrode possesses low electrical contact and charge-transfer resistances. Meanwhile, large Warburg diffusion tails imply the electrode possesses excellent ion mobility performance. After fully discharging, the electrode shows an elevated resistance (240 Ω) due to the formation of non-conductive Li_2CO_3 on the surface of the electrode. It is worth noting that the semicircle diameter becomes smaller after the device fully recharges (180 Ω) due to the decomposition of Li_2CO_3 under the presence of the Ru catalyst. These results reveal that the Ru/CNF electrode features high electrical conductivity and catalytic activity, as well as a porous structure, making it a favorable candidate for capturing CO_2 and enabling the development of commercially viable, rechargeable energy-storage devices.

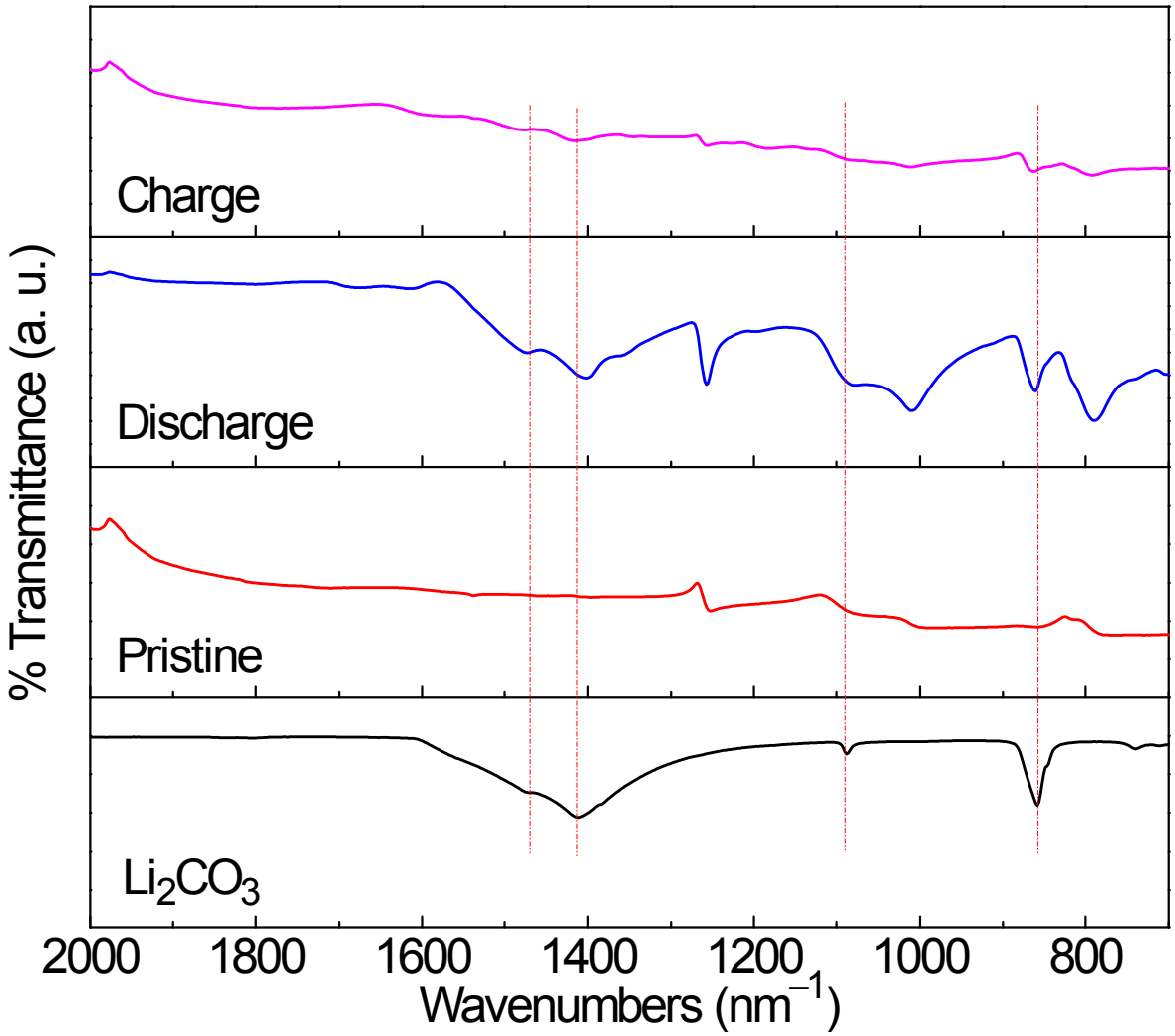

Figure S14. FTIR spectra of Li_2CO_3, the pristine Ru/ACNF electrode, the cycled electrode after discharge and recharge, to prove the deposition of Li_2CO_3 in the discharge process and its decomposition after recharge.